ELSEVIER

Power-to-melts of uranium–plutonium oxide fuel pins at a beginning-of-life condition in the experimental fast reactor JOYO

Masaki Inoue *, Kazuya Yamamoto, Takashi Sekine, Masahiko Osaka,
Naoya Kushida, Takeo Asaga

*Oarai Engineering Center, Japan Nuclear Cycle Development Institute, 4002 Narita-cho, Oarai-machi, Higashi-ibaraki-gun,
Ibaraki-ken 311-1393, Japan*

Abstract

Power-to-melts of uranium–plutonium oxide fuel pins at an initial startup condition were experimentally obtained from the B5D-2 test in the experimental fast reactor JOYO in Oarai Engineering Center. MCNP code calculations were combined with burnup measurements to determine linear heat rating of the test fuel pins. To identify the axial incipient melting positions corresponding to the power-to-melts, solidified grain morphology and molten fuel axial movements were characterized. Extensive observations on longitudinal ceramographs allowed classifying molten fuel settlements near bottom and top extents of axial fuel melting into three types. The power-to-melts depended slightly on fuel-to-cladding gap sizes and clearly on both oxygen-to-metal ratios and densities of fuel pellets. These dependencies resulted from the fuel pellet cracking and relocation behavior, which fairly improves heat transfers across the gaps. Also, the power-to-melt at the bottom position was higher than that at the top position due to an axial gradient of cladding temperatures in each fuel pin.
© 2003 Elsevier B.V. All rights reserved.

PACS: 28.41.Bm; 28.50.Ft

1. Introduction

Uranium–plutonium oxide driver fuel pins are designed to prevent any fuel center melting at both steady state and transient conditions under the safety criteria both in the experimental fast reactor JOYO and in the prototype fast breeder reactor MONJU. For this thermal aspect, power-to-melt experiments can provide two pieces of essential information to understand fuel pin thermal performances at higher temperatures. One is a 'temperature-indexed data set', since at an axial incipient melting position the fuel center is equal to be the fuel melting point (solidus temperature) and cladding temperature is also known. It can be very preferable to verify and/or calibrate fuel pin thermal performance analysis codes. The other is the allowable maximum pin power, which is experimentally demonstrated for a certain fuel pin specification. Since it is hardly attainable to irradiate a large number of fuel pins with entire specification ranges, the temperature-indexed data sets are much more useful in practice.

At a beginning-of-life condition, specifically say, at an initial startup, the fuel pellet usually experiences the highest temperature which induces significant fuel restructuring at higher local linear heat rating, LHR (pin power) than 30 kW/m. However, reports and publications of power-to-melt experiments at beginning-of-life conditions were very limited. Actually, only the results

* Corresponding author. Tel.: +81-29 267 4141x5713; fax: +81-29 267 1676/7130.

E-mail address: minoue@oec.jnc.go.jp (M. Inoue).

of the 'P19' and 'P20' tests in the EBR-II [1], the 'DEA-2' test in the FFTF [2], and the 'POTOM' tests in the HFR [3] can be found in the literatures.

In 1990s, a series of power-to-melt tests named as 'B5D-1 (PTM1)' and 'B5D-2 (PTM2)' particularly at initial startup conditions were conducted in the JOYO. The B5D-1 test was the first and preliminary experiment with only four test fuel pins prior to the B5D-2 test which was the second and main one. In the B5D tests, fuel-to-cladding gap size, fuel pellet density, fuel pellet stoichiometry, and filling gas composition were selected as test parameters. It should be emphasized that fuel pellet characterizations, pin power determinations, and post-irradiation examination technique developments were concurrently performed after the irradiations. Therefore, both pin power determinations and post-irradiation examination techniques in the B5D-2 test were much more improved than those in the B5D-1 test. Experimental results of the B5D-1 test have been already reported in Refs. [4,5]. Consequently, this paper focuses only the B5D-2 test results.

In this paper, firstly, the basic test design and experimental procedures of the B5D-2 test are described. Secondly, MCNP code (Monte Carlo code) calculations are combined with burnup measurements to determine LHR of 24 test fuel pins. Thirdly, on the basis of post-irradiation examination results including ceramographs and electron probe microanalysis (EPMA), we characterize microstructure features and molten fuel axial movements to accurately identify the axial incipient melting positions; each corresponds to the power-to-melt. Finally, the effects of fuel pellet specifications and irradiation behavior on the power-to-melts are investigated to understand fuel pin thermal performances at beginning-of-life conditions.

2. Outline of the B5D-2 test

2.1. Basic test design of the B5D tests

With reference to design studies of large scale fast breeder reactors in the middle of 1980s, a standard fuel pin specification was provisionally determined for the B5D tests [4,6]. Cladding material was the advanced austenitic steel (15Cr–20Ni stainless steel); an outer diameter and a wall thickness were 7.5 and 0.4 mm, respectively. Density, plutonium fraction (Pu/(U + Pu)), and oxygen-to-metal (O/M) ratio of the fuel pellet were 92%TD, 0.2, and 1.97, respectively. The resultant nominal fuel-to-cladding diameter gap size was 180 μm.

In the B5D tests, fuel-to-cladding gap size (three levels), fuel pellet density (two levels), fuel pellet stoichiometry (three levels), and filling gas composition (two kinds) were selected as test parameters to the standard fuel pin specification. Twenty-four test fuel pins were

manufactured with test variations actualized by fuel pellet lots and tag gas capsules.

A rapid linear power increase without pre-conditioning to the maximum power was selected for the startup mode from a view of the reactor operation similarly to that (stair type increase) in the DEA-2 test [2]. By contrast, the EBR-II tests [1] were pre-conditioned at about 90%.

2.2. Fuel pin manufacturing and assembling

Nagai et al. have reported the manufacturing results of the B5D-2 test fuel pins [7]. The specifications of each test fuel pin were listed in Table 1. The test fuel pins were filled with pure helium gas, and fueled with 550 mm in column length. Three fuel pins additionally contained tag gas capsules and resultant filling gas content was adjusted to He–4vol.%Kr–4vol.%Xe.

Six lots of fuel pellets, designated as 'B5D-201' through 'B5D-206', were fabricated in different outer diameter (fuel-to-cladding gap size), O/M ratio, and/or density. All fuel pellets were flat-ended, solid, and 9 mm in height, contained 19 mass% of plutonium (Pu/(U + Pu)), and were enriched in uranium-235 to 22 mass%. One standard deviation of fuel pellet outer diameters was ∼4 μm, and that of the densities was ∼0.3%TD for high-density lots (B5D-205 and B5D-206) and ∼0.7%TD for medium-density lots (B5D-201 through B5D-204). Inoue et al. have characterized the porosity distributions in the fuel pellets to experimentally determine their effects on thermal conductivity and reported in Refs. [8,9].

Every four test fuel pins were subassembled into a compartment with a temperature monitor (TED). Six compartments were assembled into an irradiation test assembly as illustrated in Fig. 1. The test fuel pins' configuration in the test assembly was optimized by thermal analysis based on the B5D-1 test results to ensure fuel center melting in all test fuel pins at the maximum power.

2.3. Reactor operation

Sekine et al. have reported the reactor operating history during the B5D-2 test in Ref. [10]. The test assembly was irradiated for 0.1596 effective full power days during 24th cycle of the JOYO in June 1992. The rate of reactor power rise from 50 MW t was 0.45 MW t/min and the reactor power was maintained at 98.5 MW t for 10 min as shown in Fig. 2. A manual scram mode was chosen for preventing additional fuel restructuring during the reactor shut down based on the ceramographic observations in the B5D-1 test.

2.4. Post-irradiation examinations

After the JOYO irradiation, the test assembly was transported to the fuel monitoring facility (FMF)

Table 1
Fuel pin specifications and pin powers in the B5D-2 test

Pin ID	Cladding outer diameter (as-fabricated) [mm], pin average	Cladding inner diameter (as-fabricated) [mm], pin average	Fuel pellet lot ID	Fuel pellet outer diameter (as-fabricated) [mm], pin average	Fuel pellet O/M ratio (as-fabricated) [–], lot mean	Fuel pellet density (as-fabricated) [%TD], pin average	Fuel pellet Pu content (Pu/(Pu + U)) (as-fabricated) [mass%], lot mean	Fuel-to-cladding diameter gap size (as-fabricated) [µm]	Tag gas	Maximum linear heat rating at DFCB = 277 mm (LHR(277)), kW/m
B5201	7.502	6.692	B5D-201	6.508	1.98	91.20	19.50	184	N	66.1
B5202	7.503	6.695	B5D-201	6.507	1.98	91.30	19.50	188	N	65.5
B5203	7.502	6.691	B5D-201	6.507	1.98	91.18	19.50	184	N	66.6
B5204	7.501	6.694	B5D-201	6.507	1.98	91.29	19.50	187	N	65.3
B5205	7.499	6.692	B5D-205	6.453	1.97	95.17	19.37	239	N	70.3
B5206	7.500	6.692	B5D-205	6.452	1.97	95.29	19.37	240	N	70.2
B5207	7.500	6.692	B5D-205	6.451	1.97	95.10	19.37	241	N	66.9
B5208	7.502	6.691	B5D-202	6.560	1.98	91.35	19.50	131	N	67.5
B5209	7.503	6.695	B5D-202	6.559	1.98	91.27	19.50	136	N	67.7
B5210	7.503	6.694	B5D-202	6.559	1.98	91.41	19.50	135	N	67.0
B5211	7.502	6.691	B5D-202	6.560	1.98	91.23	19.50	131	N	67.0
B5212	7.501	6.692	B5D-202	6.560	1.98	91.38	19.50	132	N	67.0
B5213	7.499	6.696	B5D-202	6.561	1.98	91.47	19.50	135	Y	67.6
B5214	7.499	6.695	B5D-202	6.561	1.98	91.43	19.50	134	Y	68.6
B5215	7.499	6.694	B5D-206	6.511	1.97	94.97	19.37	183	N	70.1
B5216	7.499	6.694	B5D-206	6.511	1.97	94.96	19.37	183	N	69.0
B5217	7.500	6.695	B5D-206	6.511	1.97	94.87	19.37	184	N	68.0
B5218	7.500	6.695	B5D-206	6.511	1.97	94.83	19.37	184	Y	69.3
B5219	7.498	6.694	B5D-203	6.501	1.96	91.28	19.46	193	N	65.6
B5220	7.498	6.694	B5D-203	6.501	1.96	91.58	19.46	193	N	66.5
B5221	7.500	6.696	B5D-203	6.501	1.96	91.54	19.46	195	N	67.5
B5222	7.499	6.694	B5D-204	6.558	1.96	91.27	19.46	136	N	67.6
B5223	7.500	6.693	B5D-204	6.558	1.96	91.16	19.46	135	N	68.1
B5224	7.500	6.693	B5D-204	6.557	1.96	91.38	19.46	136	N	67.0

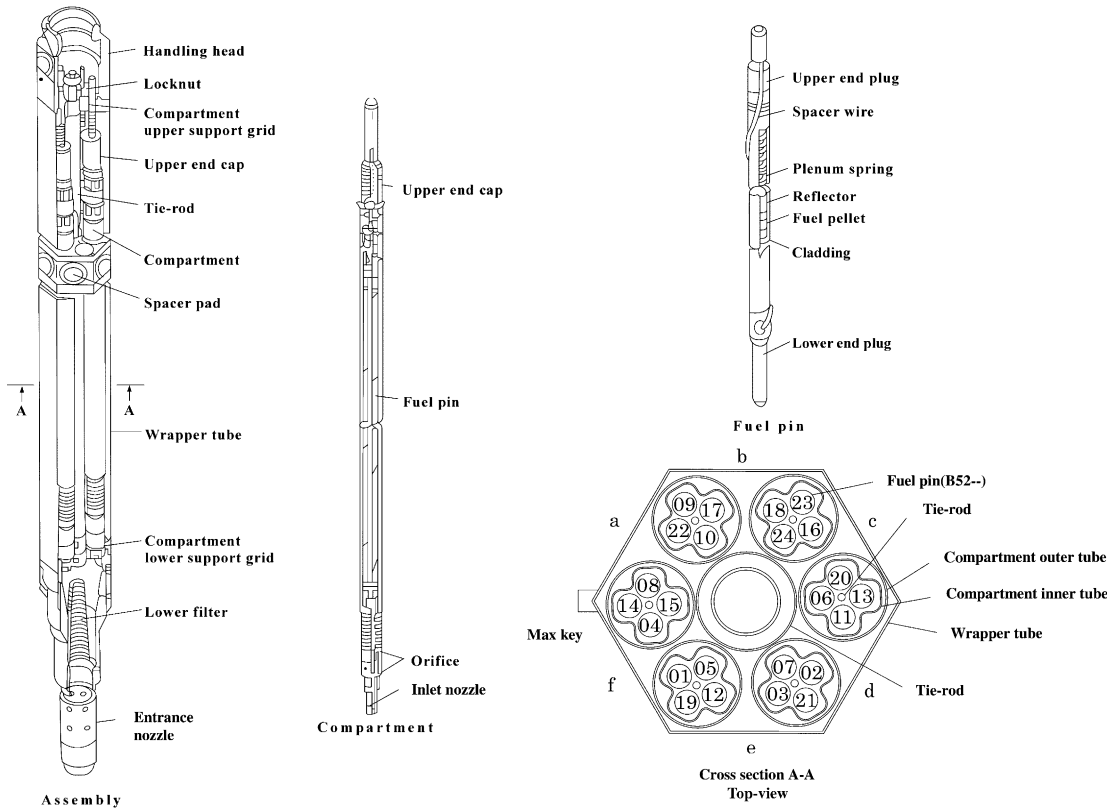*Note*: Y, loaded; N, not loaded.

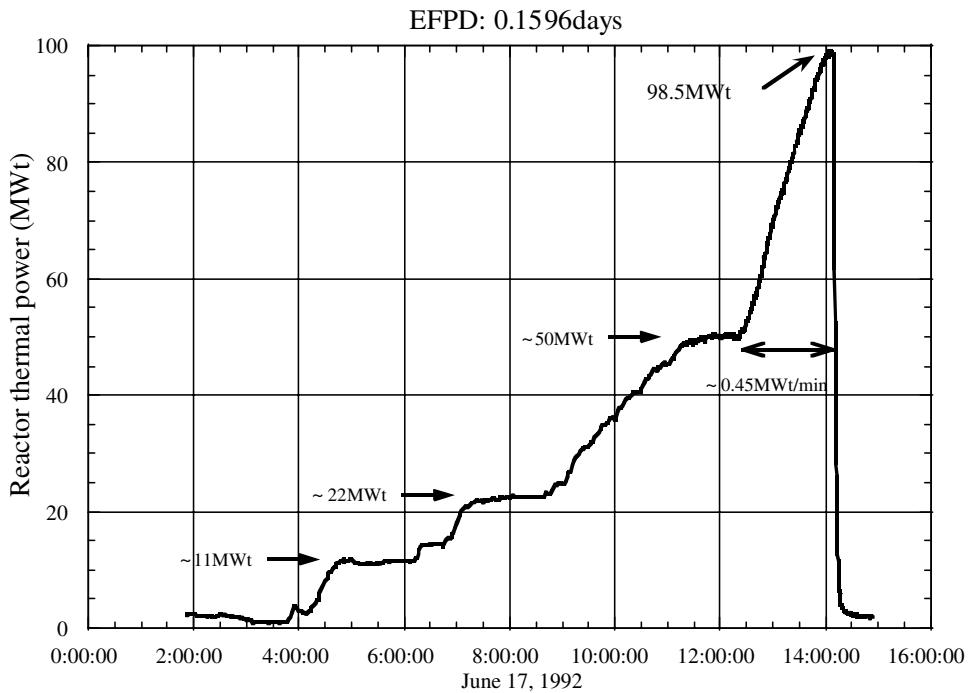Fig. 1. Schematic drawings of fuel pins and assembly irradiated in the B5D-2 test.

Fig. 2. Reactor power history of the B5D-2 test.

adjacent to the JOYO and disassembled to perform non-destructive examinations (NDEs) including X-ray radiography, weight measurements, visual inspections, cladding outer diameter profilometry, and gamma scanning for all test fuel pins. After the NDEs, the test fuel pins were punctured and sectioned to prepare specimens for optical microscopy, EPMA, and burnup measurement. Detailed descriptions of post-irradiation examination techniques can be found in Refs. [11,12].

Optical microscopy and EPMA works for both longitudinal and transverse specimens performed in the FMF characterized fuel center melting behavior to accurately identify axial incipient melting positions. For specimen preparations, central void plugging morphology in the X-ray radiographs and moving averaged zirconium-95 emitted gamma-ray intensity profile should be useful to estimate the axial range of fuel center melting. Longitudinal specimens (25 mm length) were sectioned to contain the positions (bottom or top melting extents). The specimens were chemically etched with 20 vol.% nitric acid and 40 vol.% hydrogen peroxide aqueous reagents at room temperature to accent grain boundaries.

The specimens from six test fuel pins for burnup measurements were prepared around 277 mm of distance from core bottom (DFCB) and analyzed in Alpha Gamma Facility (AGF) in Oarai Engineering Center to calibrate MCNP code calculations in pin power determinations.

3. Pin power determination

3.1. Linear heat rating of the test fuel pins

MCNP code [13] was used to evaluate the LHR of 24 test fuel pins within the test assembly. In MCNP calculations, whole core geometry was simulated. Fig. 3 shows the geometry model of the test assembly and a JOYO MK-II driver fuel assembly. The local neutron flux distribution within the test assembly was calculated using exact three-dimensional modeling of the test assembly. The fuel composition and the neutron source distribution of each driver fuel assembly were calculated using the JOYO MK- II core management code system MAGI [14], which was based on three-dimensional diffusion theory with seven neutron energy groups, and were inputted into MCNP. In MCNP calculations, the homogeneous driver fuel assembly was modeled in Hex-Z as it was in MAGI. Regarding the calculation accuracy of MAGI, the burnup fraction of the driver fuel by MAGI agreed with the measured values within 5%.

Using precise three-dimensional modeling of the test assembly, neutron flux of each test fuel pin was calculated. The detailed calculation method is described in Table 2. FSXLIB-J3R2 cross section library [15], which was processed from JENDL-3.2, was used. The plutonium-239 Watt type fission spectrum was used as an energy distribution representing the MOX fuel content. Neutron flux was calculated using track length estima-
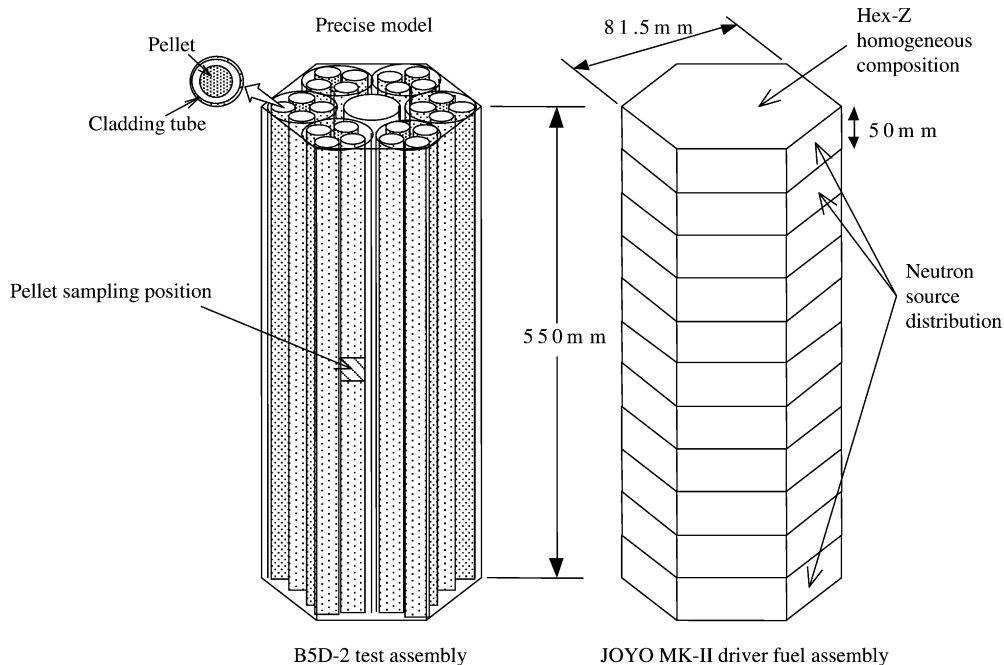

Fig. 3. Geometry models of the B5D-2 test assembly and a JOYO MK-II driver fuel assembly.

Table 2
Specific conditions of MCNP calculations

Geometry	B5D-2	Precise configuration
	Other subassembly	Hex-Z (homogeneous)
Neutron source distribution	B5D-2	Fission neutron by MCNP
	Other subassembly	Calculated by MAGI
Neutron cross section	FSXLIB (based on JENDL-3.2)	
Fission spectrum	Watt type fission spectrum (induced fission spectrum of ^{239}Pu, in case that incident neutron energy is 1 MeV)	
Number of history	2.0E+07 ($1\sigma \fallingdotseq 1\%$)	

tion tally (F4 tally). Fission rates of each fuel nuclide were derived from neutron flux calculations and fission cross sections. The LHR was evaluated using fission rates and energy generated per fission of each fuel nuclide. The ratio of the gamma energy containing delayed gamma was evaluated using MAGI calculations.

The calculation accuracy was confirmed using the fission rate based on the neodymium-148 production measurement. Neodymium-148 is one of the stable fission products, and its fission yield which is used from JNDC-V2 [16] is highly reliable. Therefore, the neodymium-148 production determined by the destructive examination has been commonly used as a burnup index.

Comparison of measured fission rates and MCNP calculations is shown in Table 3. The average ratio of the calculated to experimental (C/E) values was 0.953. This result indicated that MCNP calculates the fission rate

Table 3
Comparison of calculated and experimental fission rates

Pin ID	Fission rate ($\times 10^{19}$ fissions/s/m^3)		Calculated/Experimental
	Calculated	Experimental	
B5214	6.20	6.67	0.929
B5208	6.20	6.57	0.944
B5215	6.59	6.94	0.949
B5204	6.26	6.46	0.969
B5218	6.48	6.86	0.945
B5207	6.61	6.75	0.979
		Average	0.953

distribution precisely. The LHR at DFCB = 277 mm (LHR(277)) was obtained from fission rates and energy generated per fission and noted in the right end column in Table 1. The calculated LHR was corrected by the averaged C/E ratio. The maximum LHR at near core mid-planes loaded with the medium- and high-density lots ranged from 65 to 69 kW/m and from 67 to 70 kW/m, respectively.

Statistical errors (1σ) in MCNP calculation, fission energy of fissile material, neodymium-148 measurement, and the averaged C/E ratio were 1%, 0.25%, 1%, and 0.78%, respectively. Therefore, random uncertainty of the pin powers was determined to be 1.6% in one standard deviation. Systematic uncertainty of the pin powers originates in that of the reactor thermal power. So, we reassessed uncertainty of the reactor thermal power with reference to the assessment by Yokoyama and Ishikawa [17], and it was determined to be smaller than 3.5% in the sum of systematic and 99.7% confidence (3σ) random components. Uncertainty of the pin powers was determined to be smaller than 6.0% in the sum of systematic and 99.7% confidence random components.

3.2. Axial pin power profile

An axial pin power relative profile of fourth order polynomial equation was derived from a regression method by use of zirconium-95 emitted gamma-ray intensities measured at five axial positions (6000 s/position) in the B5212 fuel pin, which showed the smallest perturbation due to molten fuel axial movements. The profile was expressed as Eq. (1):

$$F = a + b \times DFCB + c \times DFCB^2 + d \times DFCB^3 + e \times DFCB^4, \qquad (1)$$

where F is correction factor (F is equal to 1 at DFCB = 277 mm), DFCB is distance from core bottom in mm, a is 0.67321, b is 2.0764×10^{-3}, c is 3.4043×10^{-7}, d is -1.7472×10^{-8}, e is 1.6449×10^{-11}. The LHR at a desired axial position can be calculated by multiplying the factor (F) and the local LHR at DFCB = 277 mm, LHR(277).

4. Fuel center melting behavior

Typical ceramographs (photo-mosaics) taken before and after chemical etching at near core mid-plane were shown in Fig. 4. In the as-polished condition (before chemical etching) shown in Fig. 4(a), central void, pore free structure, columnar grains, and unrestructured region (as-fabricated structure) were observed sequentially from its geometric center. After chemical etching shown
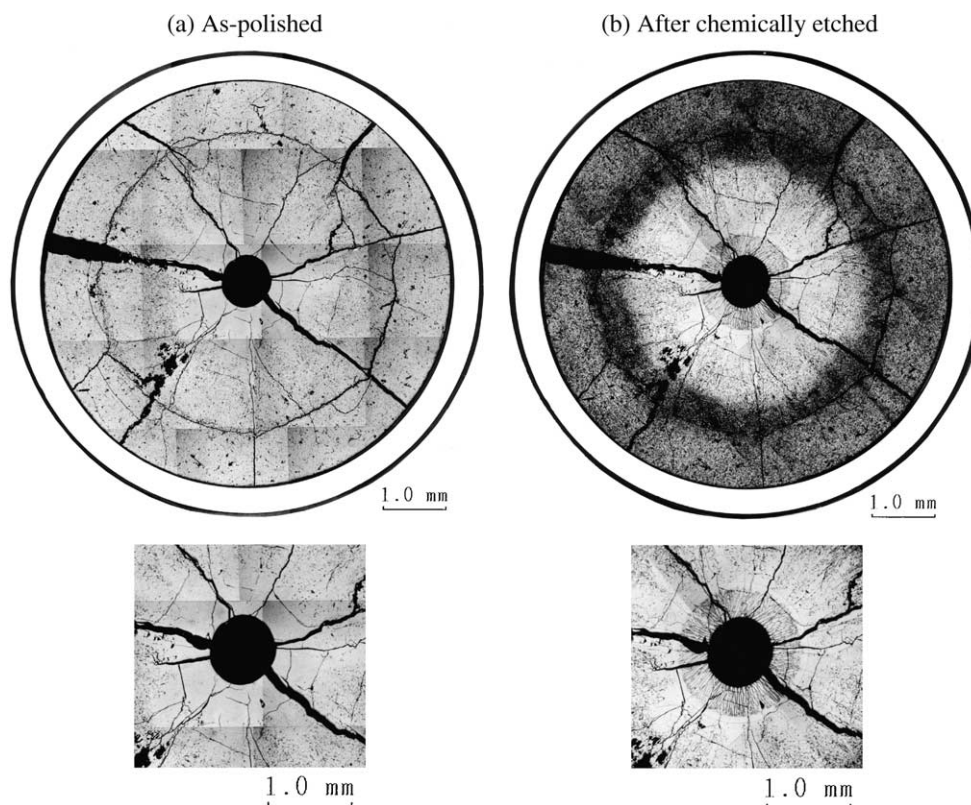
(a) As-polished

(b) After chemically etched

Fig. 4. Transverse ceramographs at near core mid-plane in as-polished (a) and after chemically etched (b) conditions in the B5216 pin.

in Fig. 4(b), the pore free structure was subdivided into dendrites and coarse grains. Microstructure features observed in 27 transverse ceramographs from all test fuel pins were summarized in Table 4.

Prior to identifying axial melting extents, we recharacterized that dendrites and coarse grains in the pore free structure were the solidified microstructure; in other words: fuel melting indicator. Radial plutonium intensity profile was measured and compared with a secondary electron image in Fig. 5. The plutonium intensity decreases in the coarse grains and then increases in the dendrites. Although profile discontinuity at the boundary between molten and unmolten fuel was observed in the POTOM-3 test [18], it was not apparent in the B5D-2 test. The urania–plutonia phase diagram indicates that urania rich phase solidifies earlier than plutonia rich liquid phase. Therefore, the plutonium intensity profile is consistent with the solidification phenomena. Definitely, neither as-fabricated nor lenticular pores were observed in both dendrites and coarse grains. By contrast, both were left in the columnar grains. As described above, plutonium radial migration behavior and pore distribution change proved that the outer surface of coarse grains or pore free structure can be defined as the extent (boundary) of fuel melting.

Comparisons with X-ray radiographs, gamma scan profiles, and longitudinal and transverse ceramographs confirmed that fuel center meltings were successfully induced in all test fuel pins. Molten fuel axial movements completely erased fuel melting indicators in seven ceramographs and plugged the central voids in five ceramographs. Fuel melting area fractions were calculated and also listed in Table 4, while the central void inner surface was assumed to be the radial extent in case with no fuel melting indicator. The maximum fuel melting area fraction of 11.8% was lower than 20% and met the safety criteria for the B5D tests. Dendrites were observed only in larger amount of fuel melting area fraction than 6%.

5. Identification of axial incipient melting positions

In identifying axial melting extents and axial incipient melting positions, a molten fuel axial movement behavior requires the careful considerations. It is very fortunate that extensive observations and morphological characterizations on longitudinal ceramographs allowed classifying molten fuel settlements near the extents. Top extents were classified into type A and B; bottom extents

Table 4
Microstructure features and molten fuel area fractions observed in the transverse ceramographs

Pin ID	Axial locations (DFCB), mm	Local maximum power[a], kW/m	Central void	Pore free structure	Dendrite	Coarse grain	Fuel melting area fraction[b], %
B5201	272	66.2	Y	N	N	N	3.0
B5202	270	65.6	Y	Y	N	Y	4.7
B5203	271	66.7	Y	N	N	N	3.4
B5204[c]	272	65.4	Y	Y	–	–	10.5
B5205	271	70.4	N	Y	Y	Y	9.2
B5206	270	70.3	Y	Y	Y	Y	10.0
B5207[c]	272	67.0	N	Y	–	–	7.4
B5208[c]	271	67.6	Y	N	–	–	3.6
B5209	270	67.8	Y	N	N	N	3.1
B5209	313	66.3	Y	Y	N	Y	5.3
B5210	270	67.1	Y	Y	N	Y	4.5
B5211	271	67.1	Y	N	N	N	3.4
B5212	270	67.1	Y	Y	N	Y	3.0
B5213	271	67.7	Y	N	N	N	2.3
B5214[c]	270	68.7	Y	Y	–	–	8.5
B5215	271	70.2	N	Y	–	–	5.1
B5216	270	69.1	Y	Y	Y	Y	6.7
B5217	272	68.1	N	Y	Y	Y	7.7
B5218[c]	270	69.4	Y	Y	–	–	6.7
B5219	271	65.7	Y	Y	Y	Y	6.6
B5220	246	66.8	Y	Y	Y	Y	11.8
B5220	271	66.6	Y	N	N	N	4.3
B5221[c]	271	67.6	Y	N	–	–	7.2
B5222	270	67.7	Y	N	N	N	2.7
B5222	306	66.5	Y	Y	Y	Y	8.1
B5223	271	68.2	N	Y	Y	Y	10.7
B5224	271	67.1	Y	Y	Y	Y	8.5

Note: Y, observed; N, not observed.
[a] The effects of axial molten fuel movements were not adjusted.
[b] Fuel melting area including central void was normalized to as-fabricated fuel pellet area.
[c] Not chemically etched.

were all the same into type C. The classifications with morphology modeling and typical longitudinal ceramographs were shown in Figs. 6–8, where the illustrations were exaggerated so that fuel pellet geometry was not exactly reproduced. The classification for every position was also listed in Table 5.

In type A, molten fuels on central void surfaces moved downwards and left enlarged central voids. Axial incipient melting positions in type A can be easily defined as the starting position where central void diameter became larger as illustrated in Fig. 6. In type B, molten fuels combined to plug the central voids. An axial incipient melting position in type B is defined as the axial position where radial melting extent is equal to its adjacent central void diameter without fuel center melting as illustrated in Fig. 7. In type C, molten fuels always plugged the central voids around bottom extents. Axial incipient melting positions in type C are defined in the

similar manner to type B as the axial position where radial melting extents are equal to the adjacent central void diameter without fuel center melting as illustrated in Fig. 8. These definitions using central void diameter extrapolations were identical to those applied in the DEA-2 test [2].

The axial incipient melting positions identified under the classifications in considering with grain morphology, plutonium intensity profile, and the moving averaged gamma-ray axial scanning profile were listed in Table 5. We failed to identify for 12 positions due to complete central void plugging, significant diameter perturbations of central voids and/or solidified structures, and technical difficulty in longitudinal specimen grinding (off to the fuel pin geometric center and inclination). Conclusively, 36 axial incipient melting positions were identified and then converted to the power-to-melts (LHR), which were noted in the right end columns in Table 5.
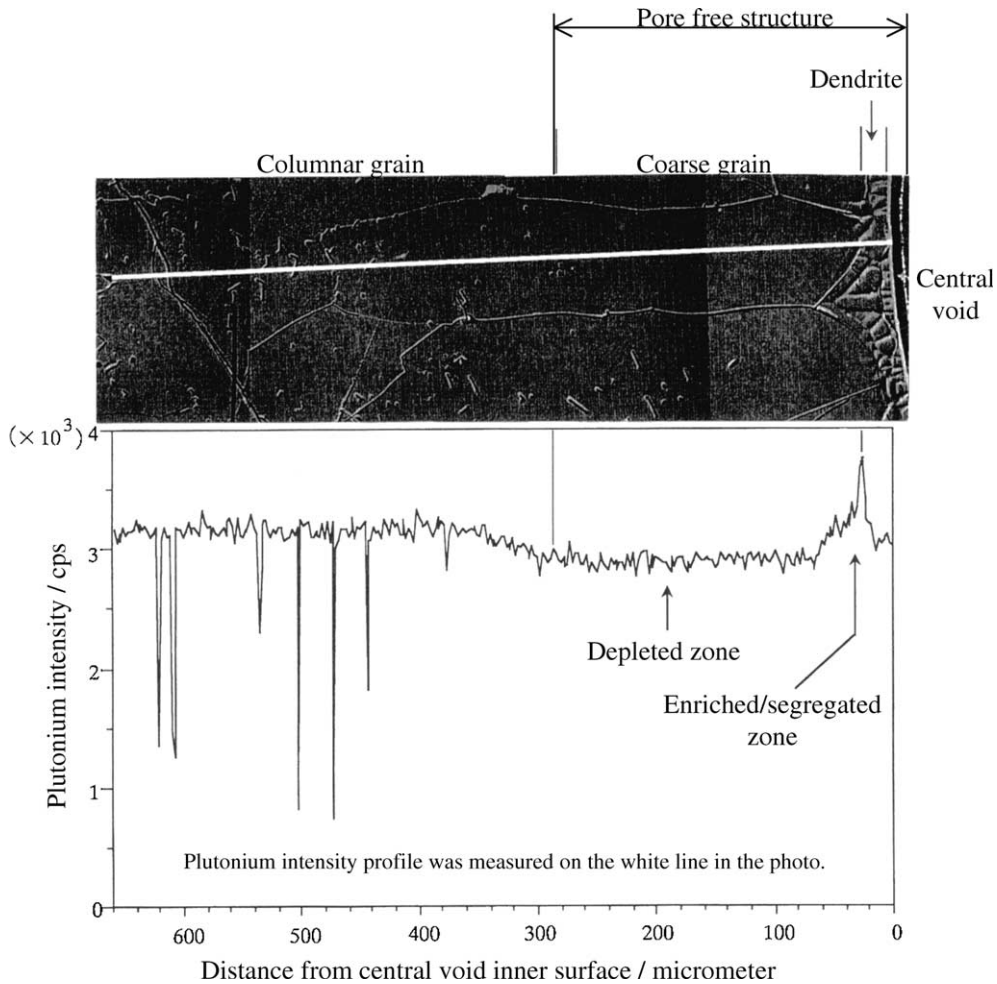
Fig. 5. Plutonium radial intensity profile compared with the grain morphology in the transverse section in the B5219 pin.

6. Effects of fuel pin specifications and irradiation behaviors on power-to-melts

The power-to-melts obtained in previous chapter are plotted versus as-fabricated diameter gap size in Fig. 9, where the LHR at the center was plotted in case that the axial incipient position was identified as the range.

Collectively in medium and high density fuel pins, it is obvious that (i) the power-to-melt at the bottom position is always higher than that at the top position due to an axial gradient of cladding temperature in each test fuel pin, that (ii) the effect of tag gas is not distinguishable, and that (iii) the lower fuel pellet density resulted in the lower power-to-melt. In the medium-density fuel pins, the power-to-melts depend, slightly on the gap size, and clearly on the O/M ratio. In the high-density fuel pins, the dependence on the gap size is not distinguishable. For comparison, power-to-melts of the P19, P20, and DEA-2 tests for FFTF driver type fuel

pins and modified ones [1,2] are summarized in Fig. 10. In contrast to the EBR-II and FFTF experiments, it is very peculiar for the B5D-2 test that the power-to-melts showed the lesser dependence on the gap size and that the effect of the filling gas composition was not distinguishable.

The dependencies of the power-to-melts on the fuel pellet specifications are discussed first. It is well known that fuel pellet cracking and relocation behavior significantly influences on both thermal and mechanical fuel pin performances particularly at beginning-of-life conditions. The relocation behavior without any fuel center melting in the JOYO experiments irradiated for shorter than four EFPDs is summarized in Fig. 11. There also exists an empirical correlation as a function of as-fabricated gap volume as written in Eq. (2):
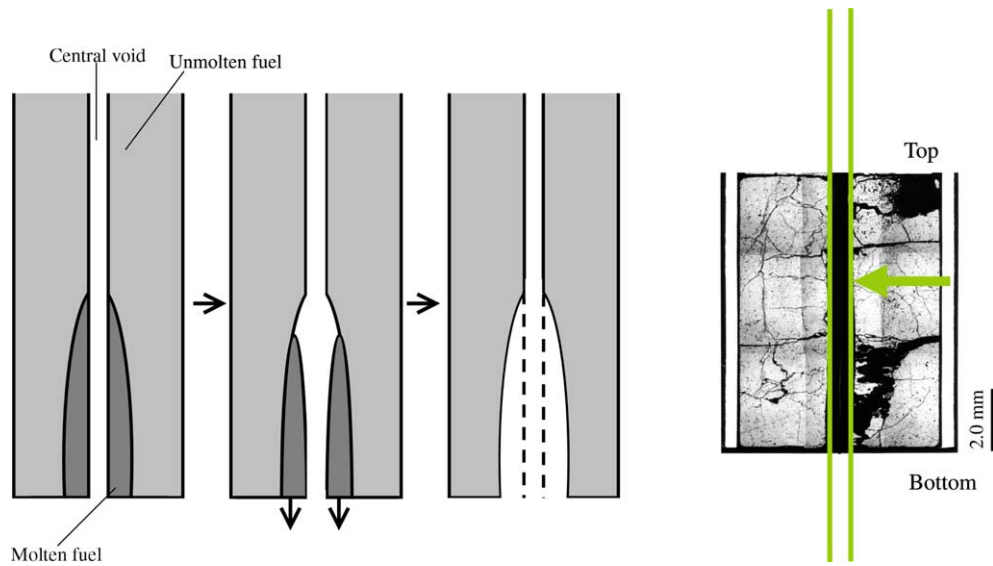
$$DR = 0.111 GR_{ci} - 45, \tag{2}$$

Fig. 6. Molten fuel axial movement behavior classified as type A at top extents in the B5206 pin.
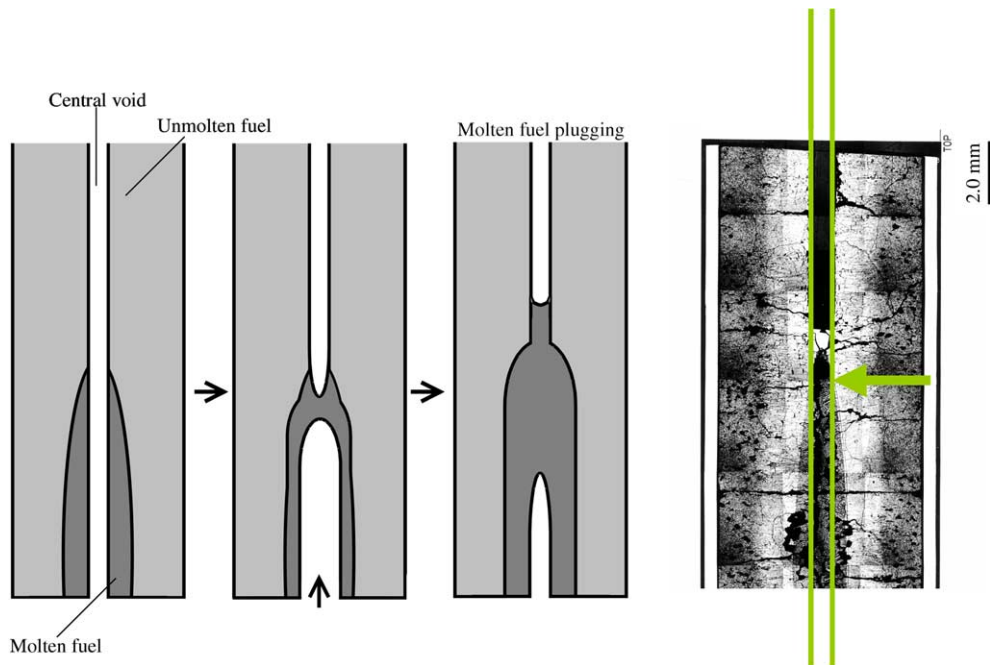

Fig. 7. Molten fuel axial movement behavior classified as type B at top extents in the B5219 pin.

where G is as-fabricated diameter gap size in μm, R_{ci} is cladding inner diameter in mm, and DR is diameter relocation in μm, one standard deviation of the predicted DR compared with the database was 19 μm [19]. The diameter relocation is defined as the difference between as-fabricated and residual diameter gap size. The residual radial gap size averaged eight measurements of distances between cladding inner surfaces and fuel pellet outer surfaces in the transverse ceramographs. As shown in Fig. 11, the relocation behavior will effectively reduce the distance (gap size) and improve the heat transfer across the gap in addition to larger thermal expansion of fuel pellet than that of cladding. As correlated in Eq. (2), the larger as-fabricated gap volume results in the larger
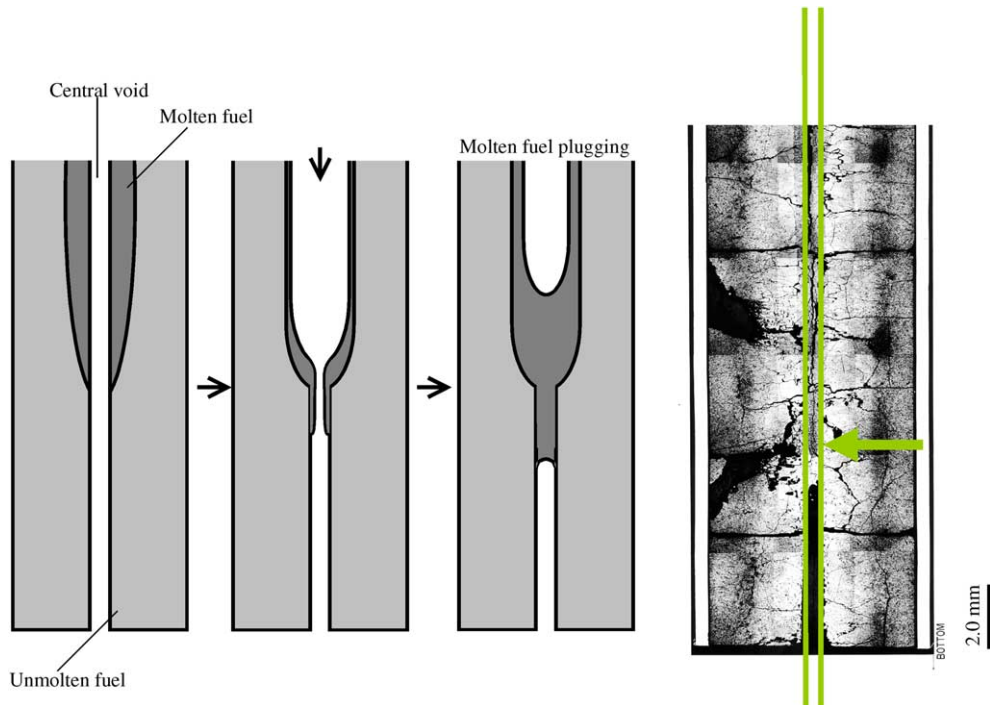
Fig. 8. Molten fuel axial movement behavior classified as type C at bottom extents in the B5205 pin.

relocation. Naturally, the relocation behavior will reduce the difference of as-fabricated gap size in the B5D-2 test. The relocation behavior can improve only the heat transfer across the gap, so it will not be effective for the heat conduction in the fuel pellet where the effect of O/M ratio and density are dominant. We conclude that the dependencies resulted from the relocation behavior. In addition to the relocation behavior, the smaller relative gap size, which is defined as the ratio of diameter gap size to cladding inner diameter, of the provisional standard fuel pin made itself less effective in the B5D-2 test when compared with the EBR-II and FFTF experiments.

The absence of the filling gas composition effect is discussed below. In case of the B5D-2 test fuel pins, temperature increments in the fuel pellet (ΔT_{fuel}) will be much larger than that across the gap (ΔT_{gap}); actually calculated $\Delta T_{fuel}/\Delta T_{gap}$ ratios ranged from 10 to 27 as reported in Ref. [5]. Even if the pure helium filled fuel pins loaded with B5D-202 lot, the scatter of the power-to-melts was about 1% (one standard deviation) in both bottom and top locations. Since at the axial incipient melting positions both fuel center and cladding inner temperatures should be almost constant, 1% change of the local LHR results in greater than 10% increase or decrease of the ΔT_{gap}. Conversely, 20% change of ΔT_{gap} results in smaller than 2% change of ΔT_{fuel}. As the tag gas addition reduces the gap gas thermal conductivity only by approximately 20%, the randomness of heat transfer and conduction inside test fuel pins will overshadow the gap gas thermal degradation due to the tag gas addition.

It is noteworthy that at both bottom and top positions the power-to-melts in the narrow gap size fuel pins loaded with B5D-202 and B5D-204 showed very small scatters. Also, the smaller as-fabricated gap size resulted in the smaller scatter of the relocation in the B5D tests as shown in Fig. 11(c). These scattering features especially in the narrow gap size fuel pins indicate that the heat transfer and conduction inside the test fuel pins are very reproducible and preferable for the verification of thermal modeling and its applicability for the fuel pin thermal analysis. Heat generation in the fuel pellet matrix is homogeneous (no radial power depression) corresponding to the radial neutron flux distribution in the B5D tests, so it gives further preferences for thermal analysis.

7. Conclusions

The power-to-melts of the uranium–plutonium oxide fuel pins under the rapid reactor startup mode without pre-conditioning were experimentally obtained from the B5D-2 test in the experimental fast reactor JOYO.

Table 5
Identifications and classifications of axial incipient melting positions for both bottom and top extents

Pin ID/axial designation	Type of molten fuel axial movement (classification)	Identified axial incipient melting position (DFCB), mm	Fuel pellet number included in the identified position	Linear heat rating at the incipient melting position (power-to-melt), kW/m
B5201B	C	–	–	–
B5202B	C	196	1	64.6
B5203B	C	165	1	63.9
B5204B	C	–	–	–
B5205B	C	157	1	66.8
B5206B	C	128–132	1	64.1–64.4
B5207B	C	–	–	–
B5208B	C	164–168	1	64.6–65.0
B5209B	C	–	–	–
B5210B	C	187	1	65.6
B5211B	C	176–190	2	65.0–65.8
B5212B	C	181	1	65.2
B5213B	C	–	–	–
B5214B	C	168	1	66.0
B5215B	C	161–183	4	66.9–68.4
B5216B	C	164–170	1	66.1–66.5
B5217B	C	–	–	–
B5218B	C	159–169	2	66.0–66.7
B5219B	C	146	1	61.4
B5220B	C	128–138	2	60.7–61.6
B5221B	C	135	1	62.2
B5222B	C	162–165	1	64.6–64.8
B5223B	C	150–163	2	64.2–65.1
B5224B	C	166	1	64.3
B5201T	B	345	1	62.5
B5202T	B	349	1	61.6
B5203T	A	–	–	–
B5204T	–	–	–	–
B5205T	B	366–377	2	64.4–63.3
B5206T	A	369	1	64.1
B5207T	A	362	1	61.7
B5208T	B	362–364	2	62.3–62.1
B5209T	–	–	–	–
B5210T	B	343–344	1	63.5–63.4
B5211T	B	349	1	63.0
B5212T	B	352–355	2	62.7–62.5
B5213T	A	367	1	62.0
B5214T	B	359	1	63.6
B5215T	–	–	–	–
B5216T	B	358–369	1	64.1–63.0
B5217T	B	359	1	63.0
B5218T	B	366	1	63.6
B5219T	B	366	1	60.1
B5220T	B	370–375	1	60.6–60.1
B5221T	B	388	1	59.6
B5222T	B	–	–	–
B5223T	B	–	–	–
B5224T	B	376	1	60.5

Note: B, bottom extent; T, top extent.

MCNP code calculations with whole core geometry were combined with burnup measurements to determine the LHR of 24 test fuel pins. The maximum LHR at near core mid-planes loaded with the medium- and high-density lots ranged from 65 to 69 kW/m and from 67 to 70 kW/m, respectively.
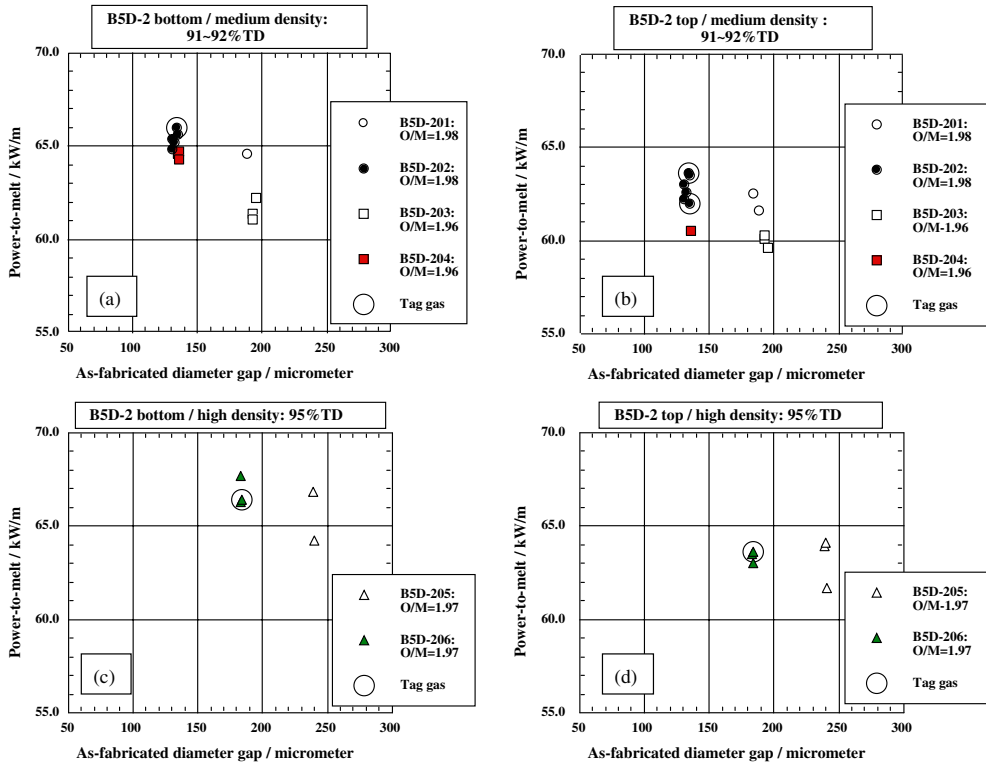
Fig. 9. Influences of fuel pin specifications on the power-to-melts in the B5D-2 test.
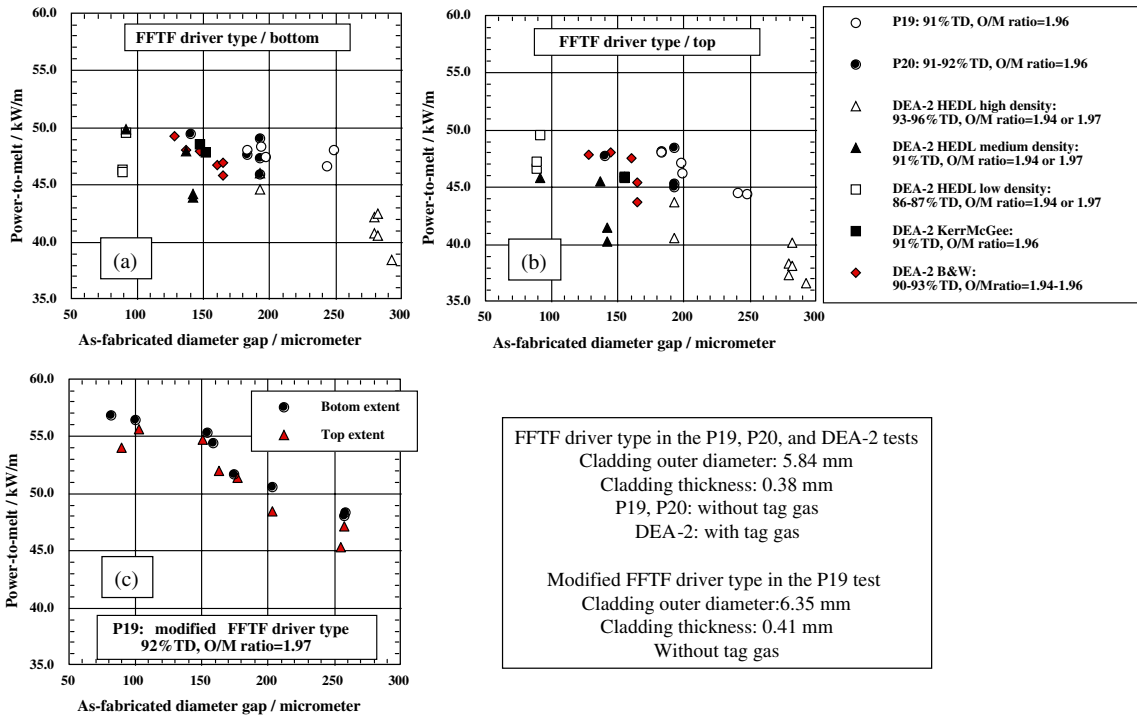

Fig. 10. Influences of fuel pin specifications on the power-to-melts in the P19, P20, and DEA-2 tests. (Data were taken from Refs. [1,2].)
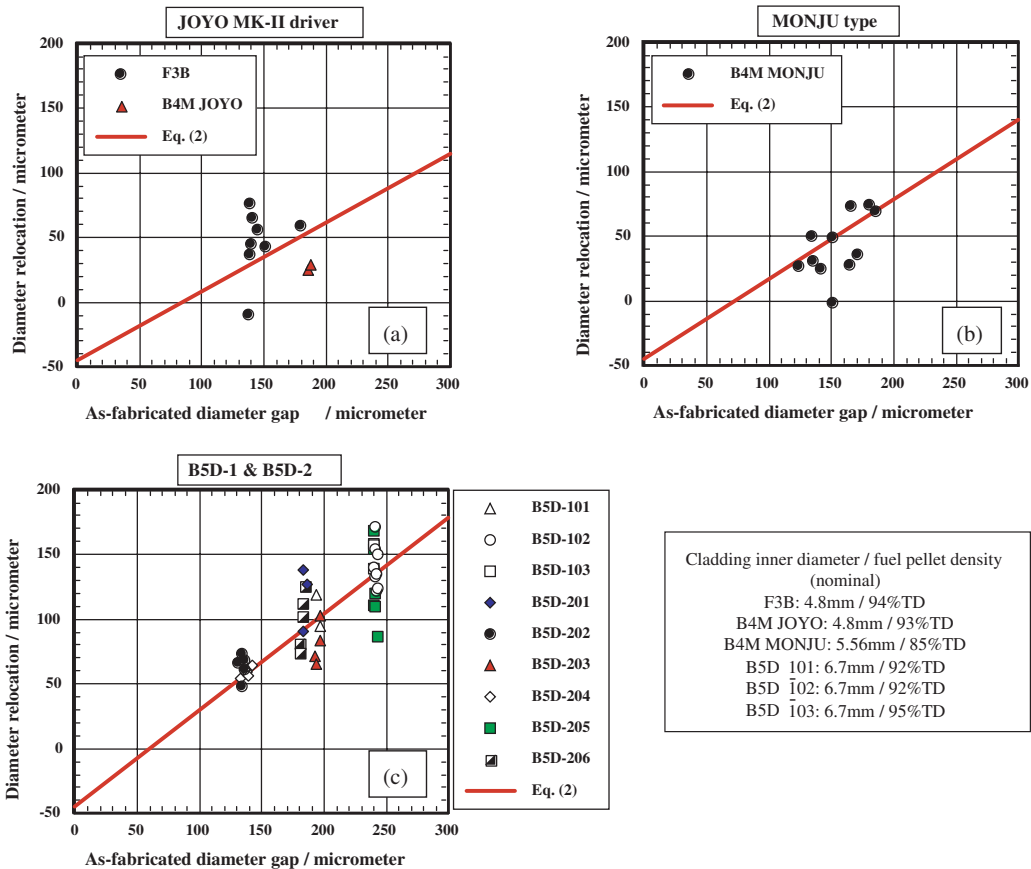
Fig. 11. Fuel pellet relocation behavior at the beginning-of-life conditions in the JOYO MK-II driver, MONJU type, and B5D tests fuel pins.

Fuel center melting behavior including solidified grain morphology and molten fuel axial movements were characterized by transverse ceramographs. Extensive observations on longitudinal ceramographs allowed classifying molten fuel settlements near bottom and top extents of axial fuel melting into three types. These classifications provided a criterion for identifying the axial incipient melting positions.

The power-to-melts depended slightly on fuel-to-cladding gap sizes and clearly on both O/M ratios and densities of fuel pellets. Also, the power-to-melt at the bottom position was higher than that at the top position due to axial gradient of the cladding temperatures, and the effect of tag gas was not distinguishable. The lesser dependence on the gap size resulted from the fuel pellet relocation behavior which fairly improves heat transfers across the gaps.

The power-to-melts data obtained from this work will be eligible to verify thermal modeling and its applicability in fuel pin thermal performance analysis codes in future.

Acknowledgements

References

[1] R.B. Baker, R.D. Leggett, in: Proceedings of International Conference on Fast Breeder Reactor Fuel, Monterey, CA, USA, March 1979, p. 258.
[2] J.L. Ethridge, R.B. Baker, in: Proceedings of Eighth International Conference on Heat Transfer, San Francisco, CA, USA, vol. 5, August 1986, p. 2485.
[3] D. Freund, D. Geithoff, H. Steiner, J. Nucl. Mater. 204 (1993) 228.
[4] S. Miyakawa, R. Kitamura, K. Soga, H. Someya, E. Kagota, Y. Sawahata, Y. Takatsudo, K. Okamoto,

T. Yasu, M. Soroi, H. Kataoka, Power Reactor and Nuclear Fuel Development Corporation Report, PNC Techn. Rev., vol. 104, 1997, p. 67 (in Japanese).

[5] M. Inoue, T. Asaga, Japan Nuclear Cycle Development Institute Report, JNC TN9400 2001-080, 2001 (in Japanese).

[6] M. Katsuragawa, H. Kashihara, M. Akebi, J. Nucl. Mater. 204 (1993) 14.

[7] S. Nagai, K. Kamimura, N. Tobita, M. Toyoshima, N. Kato, Y. Nogami, K. Isaka, S. Ishida, K. Onuma, M. Ohtsu, Power Reactor and Nuclear Fuel Development Corporation Report, PNC TN8410 93-030, 1992 (in Japanese).

[8] M. Inoue, T. Asaga, Japan Nuclear Cycle Development Institute Report, JNC TN9400 99-005, 1998 (in Japanese).

[9] M. Inoue, K. Abe, I. Sato, J. Nucl. Mater. 281 (2000) 117.

[10] T. Sekine, R. Kitamura, T. Aoyama, Japan Nuclear Cycle Development Institute Report, JNC TN9400 2000-071, 2000 (in Japanese).

[11] K. Yamamoto, N. Kushida, A. Koizumi, Japan Nuclear Cycle Development Institute Report, JNC TN9400 2000-029, 1999 (in Japanese).

[12] K. Yamamoto, N. Kushida, Japan Nuclear Cycle Development Institute Report, JNC Techn. Rev., vol. 11, 2001, p. 105 (in Japanese).

[13] J.F. Briesmeister, Los Alamos National Laboratory Report, LA-12625-M, 1993.

[14] S. Maeda, T. Sekine, T. Aoyama, in: Transactions of 5th International Topical Meeting on Research Reactor Fuel Management (RRFM 2001), Eurogress Aachen, Germany, 1–3 April 2001, p. 56.

[15] K. Kosako, F. Maekawa, Y. Oyama, Y. Uno, H. Maekawa, Japan Atomic Energy Research Institute Report, JAERI-DATA-CODE-94-20, 1994.

[16] K. Tasaka, J. Katakura, H. Ihara, T. Yoshida, S. Iijima, R. Nakashima, T. Nakagawa, H. Takano, Japan Atomic Energy Research Institute Report, JAERI 1320, 1990.

[17] K. Yokoyama, M. Ishikawa, Japan Nuclear Cycle Development Institute Report, JNC TN9400 2000-061, 2000 (in Japanese).

[18] H. Kleykamp, J. Nucl. Mater. 294 (2001) 8.

[19] M. Inoue, S. Ukai, T. Asaga, Japan Nuclear Cycle Development Institute Report, JNC TN9400 99-070, 1999 (in Japanese).